Research Paper

Potential reactivity assessment of mechanically activated kaolin as alternative cement precursor

J. Mañosa [a], A.M. Gómez-Carrera [a], A. Svobodova-Sedlackova [a], A. Maldonado-Alameda [a], A. Fernández-Jiménez [b], J.M. Chimenos [a],[*]

[a] Departament de Ciència de Materials i Química Física, Universitat de Barcelona, C/Martí i Franquès 1, 08028 Barcelona, Spain
[b] Instituto de Ciencias de la Construcción Eduardo Torroja (IETcc), CSIC, C/Serrano Galvache 4, 28033 Madrid, Spain

ABSTRACT

This work aims to assess the potential reactivity of a mechanically activated kaolin for its use as an alternative cement precursor. The mechanical activation was successfully achieved by grinding at different rotation speeds (250, 300, and 350 rpm) and times (60, 90, and 120 min), obtaining a highly amorphous and reactive material. The amorphization was monitored through XRD with amorphous content estimation and FTIR deconvolution. The potential reactivity was evaluated through chemical attacks, obtaining SiO_2 and Al_2O_3 availabilities up to 95 wt% and 93 wt% of total SiO_2 and Al_2O_3 content. XRD and FTIR also allowed the identification of the non-reactive phases on the insoluble residue after chemical attacks. NMR analysis revealed that part of the aluminium was in IV coordination, limiting the reactivity in the alkali activation process. This work demonstrated the effectiveness of mechanical activation as a greener treatment than thermal dehydroxylation to increase the raw kaolin's reactivity.

1. Introduction

Clays and clay minerals have been used since antiquity for their variety of properties and abundance worldwide. In ancient times, clays were used in a wide range of applications (e.g. construction, pottery and art). Nowadays, clays are essential materials in multiple sectors, from domestic uses to high-tech applications, because of their diverse structures and properties, being the raw materials of all kinds of products (Daou et al., 2020). In the ceramic industry, clays are used to produce bricks, tiles, and porcelain. But they are used to create products in other sectors, such as paper, plastics, cosmetics, catalysts and adsorbents, among others (Bergaya and Lagaly, 2006; Ondruška et al., 2018). However, in the construction industry, clays have lost relevance in front of cement and concrete. Although cement is the main product in the construction sector, clays can be used in conventional cement (ordinary Portland cement, OPC) production, both as a precursor during clinkering and pozzolanic material. Because of its composition, clinker requires high-temperature calcination before its use (more than 1400 °C), causing cement manufacturing to be one of the most polluting industrial processes. In this sense, to address this issue, the OPC incorporates different percentages of supplementary cementitious materials (SCMs)

such as natural pozzolans, fly ashes, bottom ashes, and blast furnace slags, among others (Lothenbach et al., 2011; Sharma et al., 2021). The addition of SCMs is one of the main strategies to reduce the environmental footprint associated with cement and concrete production (Juenger et al., 2019). SCMs also increase concrete strength through pozzolanic reactions (Juenger and Siddique, 2015). Furthermore, seeking alternative cementitious materials (ACMs) is crucial to reduce even more the carbon footprint in the cement industry (Scrivener and Kirkpatrick, 2008). The most studied ACMs are calcium aluminate cement (CAC), calcium sulphoaluminate cement (CSAC), belite cement, and alkali-activated binders (AABs), among others (Juenger et al., 2011). The recent progress on ACMs is mainly focused on using waste and by-products as precursors to give a second life to a residue contributing to the circular economy (Shi et al., 2019). However, waste and by-products are not extensively available everywhere, and their amount cannot meet the demand of the construction sector (Provis, 2018). In contrast, clays are abundant and globally available materials that could easily meet the demand of the cement industry and be used as cementitious materials precursors (Scrivener et al., 2018; Khalifa et al., 2020).

Clays are suitable for cement production mainly due to their high

---

SiO_2 and Al_2O_3 content and wide-ranging accessibility. In addition, their composition is appropriate for their use both as SCM and ACM precursors, especially for AABs formulations (Khalifa et al., 2020). Nonetheless, the reactivity of clay precursors is scant, and a previous activation of the material must be performed (Mañosa et al., 2021). The most common activation process is carried out through thermal process, where the clay structure undergoes a dehydroxylation stage causing the release of the hydroxyls and the amorphization of the structure (Cheng et al., 2019). Depending on the clay type and structure, thermal dehydroxylation requires temperatures between 500 °C and 900 °C. The use of thermally activated clays as SCMs and ACMs has been exhaustively studied and validated, being kaolin one of the most used clays in binder materials research (Liew et al., 2016; Yanguatin et al., 2017; Sharma et al., 2021). Kaolin has been used in many studies mainly due to its worldwide availability and composition (Khalifa et al., 2020). By heating kaolin at 550–850 °C for 1–12 h, kaolinite is amorphized into metakaolinite, obtaining the highly reactive material known as metakaolin (Rashad, 2013). However, the energy consumption during this process is an important downside in front of waste-based ACM precursors or SCMs. Therefore, the activation of the clay precursor should be achieved with lower energy-requiring procedures. In this sense, mechanical activation (MA) and chemical activation (CA) arise as feasible activation methods that could reduce the required energy compared to thermal dehydroxylation. More concretely, the energy required to obtain metakaolin via thermal treatment is around 1600 kWh·t^{-1}, while the obtention of mechanically activated kaolin is expected to be 200–1000 kWh·t^{-1}, depending on the mechanical treatment used (Fitos et al., 2015). While CA is a feasible activation method, MA is considered more simple, economical, and environmentally friendly since it does not necessarily involve solvents or chemical products (Mitrović and Zdujić, 2014). MA is a branch of mechanochemistry where chemical and physicochemical changes are induced to the treated material using mechanical energy (typically applied via grinding in a mill) (Baláž, 2008). Through grinding, the grain size is refined, the surface area of particles increases, and structural changes are originated (Akhgar and Pourghahramani, 2015). Furthermore, non-crystalline (amorphous) material is formed with highly energetic mechanical treatments (Wu et al., 2021), increasing the chemical activity of mechanically activated materials (Baláž et al., 2013).

Mechanical activation of kaolinite has been found to reduce the particle size and increase the specific surface area of the material, although intensive treatments cause agglomeration of particles by cold-welding, causing particle size increase and specific surface area decrease (Souri et al., 2015). Furthermore, the kaolinite structure is disordered and even amorphized. MA also modifies the dehydroxylation temperature since the hydroxyls are separated from the structure and therefore, more easily released. Authors have reported that the parameters of the dry-grinding process highly affect the changes on kaolin. Different degrees of amorphization are achieved depending on the mill type, milling time, rotation speed (for planetary mills), and ball-to-sample ratio, among others (Tole et al., 2019). Studies have been performed on using mechanically activated kaolins to produce several materials such as zeolites, pozzolans, and geopolymers (San Cristóbal et al., 2010; Hounsi et al., 2013; Mitrović and Zdujić, 2014; Fitos et al., 2015; Derouiche and Baklouti, 2021). Balczár et al. produced geopolymers with compressive strengths even higher than metakaolin-based geopolymers (Balczár et al., 2016). However, there are very few studies focusing on understanding how structural modifications induced through mechanical activation affect kaolin's reactivity.

This work aims to evaluate the potential reactivity of mechanically activated kaolin compared to raw kaolin and metakaolin, mainly for its use as SCM or ACM precursor. To fulfil this objective, a comprehensive analysis of raw kaolin, various mechanically activated kaolin, and thermally activated kaolin has been carried out to elucidate the structural changes during mechanical treatments that lead to a more reactive material. Furthermore, a reactivity analysis was performed through

alkaline chemical attacks, and the potentially reactive and non-reactive phases were determined by examining the insoluble residue.

2. Materials and methods

2.1. Materials

Commercial kaolin provided by the Spanish company Minerals i Derivats, S.A. was used as raw material in the project. The composition of the kaolin was determined through X-ray fluorescence (XRF) with a Panalytical Philips PW 2400 sequential X-ray spectrophotometer equipped with UniQuant® V5.0 software. Major elements, expressed as their most stable oxides, were silicon (49.9 wt% of SiO_2) and aluminium (36.3 wt% of Al_2O_3), while the loss on ignition (LOI) at 1100 °C was 12.5 wt%. The kaolin also contained minor elements as potassium and iron (0.7 wt% of K_2O and 0.5 wt% of Fe_2O_3, respectively). The main crystalline phases, detected through X-ray diffraction (XRD) using a Bragg-Brentano PANalytical X'Pert PRO MPD alpha1 powder diffractometer with CuKα$_1$ radiation (λ = 1.5406 Å), focalizing Ge (111) primary monochromator, step size of 0.026°, anti-scatter slit of 4°, Soller slit of 0.04 rad, measuring time of 100 s and five repeated scans. The crystalline phases detected with X'Pert HighScore software were kaolinite and quartz, while weak reflections of microcline, probably with some contribution of other potassium feldspars (such as orthoclase and sanidine), and illite were also identified.

2.2. Mechanical activation methodology

The mechanical activation (MA) process was performed using a RETSCH planetary ball mill PM 400. 10 mm zirconia balls were used as grinding bodies in zirconia grinding jars of 125 cm^3. Based on preliminary tests, the mass ratio of balls-to-sample (20) and the jars' approximate volume occupation (20%) were fixed. Three rotational speeds (250, 300, and 350 rpm) and 3 milling times (30, 60, and 120 min) were used, obtaining 9 different combinations. Based on these combinations, the nomenclature used in this work is KS-T, where K refers to the kaolin used as raw material, S stands for rotation speed in rpm, and T for milling time in min (e.g. K250–30 is kaolin ground at 250 rpm for 30 min). The same raw kaolin (K) was thermally activated (TA) at 750 °C for 6 h to obtain a reference dehydroxylated metakaolin (MK), based on previous knowledge and bibliography (Rashad, 2013). For better understanding, through the results section, usually only 2–3 of the MA samples will be presented (always together with K and MK): the less and the most aggressive mechanical treatments, K250–30 and K350–120 respectively, were selected as representative samples, and in most of the results, K300–60 will also be presented representing a moderately aggressive mechanical treatment.

2.3. Characterization

Five scans of each sample were performed to acquire representative XRD results, following the previously stated methodology. The amorphous content (W_{amorph}) in the samples was estimated to examine the potential reactivity of the activated samples using direct semi-quantitative methods: the combination of single peak method and degree of crystallinity (DOC) method (Madsen et al., 2011), through Eq. 1 and Eq. 2:

$$DOC = \frac{Crystalline\ Area}{Crystalline\ Area + Amorphous\ Area} \tag{1}$$

$$W_{amorph} = 1 - DOC \tag{2}$$

Moreover, the amorphous content was validated with one of the mechanically activated samples by Rietveld standard method (Whitfield and Mitchell, 2003), with adjustment values of $R_{wp} = 2.6$ and $\chi^2 = 1.5$.

^{27}Al and ^{29}Si magic angle spinning nuclear magnetic resonance (MAS

NMR) was performed. ^{27}Al MAS NMR spectra were recorded at RT in an AVANCEIII HD 600 (Bruker AXS) spectrometer using a triple resonance DVT probe of 2.5 mm at a spinning rate of 20 kHz. The magnetic field was 14.1 T corresponding to a [27]Al resonance frequency of 156.37 MHz. The [27]Al chemical shifts are referenced to $Al(NO_3)_3$. ^{27}Al MAS NMR spectra were recorded with a 0.27-us 90° pulse and 1-s delay with 1H decoupling ([27]Al Hpdec with cw decoupling sequence for Al) and summing up 2000 scans. ^{29}Si MAS NMR spectra were recorded at RT in an AVANCEIII HD 600 (Bruker AXS) spectrometer using a triple resonance DVT probe of 2.5 mm at a spinning rate of 15 kHz. The magnetic field was 14.1 T corresponding to a [29]Si resonance frequency of 119.22 MHz. The [29]Si chemical shifts are referenced to TMS. ^{29}Si MAS NMR spectra were recorded with a 5-us 90° pulse and 30-s delay with 1H decoupling ([29]Si Hpdec with cw decoupling sequence for Si) and summing up 8300 scans.

An ATI MATTSON FTIR-TM series spectrophotometer in transmission mode, with samples prepared by mixing 0.9 mg of sample in 200 mg of KBr, was used to study the Fourier-transform infrared spectroscopy (FTIR) spectra. This spectral analysis was performed with 32 scans over the range 4000–400 cm^{-1} at a resolution of 4 cm^{-1}. The spectra were deconvoluted in the 1300–850 cm^{-1} range with OriginPro 2021 software. The positions of the deconvolution bands were determined with the help of the second derivative function.

The potential availability of SiO_2 and Al_2O_3 was evaluated through Inductively Coupled Plasma – Optical Emission Spectroscopy (ICP-OES) on the solution resulting from chemical attacks with NaOH 8 M. 1 g of sample was dissolved in 100 mL of NaOH 8 M (S/L ratio of 1/100) and stirred for 5 h at 80 °C (Ruiz-Santaquiteria et al., 2011; Kuenzel and Ranjbar, 2019). The insoluble residue was studied through XRD with the same conditions described before and FTIR to determine the potentially reactive and the non-reactive phases. The FTIR spectra were acquired using a Nicolet 5700 FTIR spectrometer from Thermo Electron in transmission mode with a 4 cm^{-1} resolution, 32 scans and a 4000–400 cm^{-1} range. The samples were prepared by mixing 0.9 mg of sample in 200 mg of KBr.

3. Results and discussion

Fig. 1 shows the diffractograms of K, MK, and MA sample with the most intensive mechanical treatment (K350–120), where the overall variations of the diffractogram can be observed. With intense MA, the main reflections of kaolinite and illite disappeared, and the creation of an amorphous phase can be detected in the two halos centred at around 25–30 2θ° and 70 2θ°, respectively, obtaining diffractograms very similar to MK's. With less energetic mechanical treatments (K250–30 and K300–60), kaolinite was partially amorphized, and in K250–30 traces of illite were still detected. A reduction of K-feldspar and quartz reflections intensities was also observed in K350–120, while these reductions were not observed in K250–30 and K300–60. In contrast, K-feldspar and quartz remained unaltered in MK and illite was detected in its dehydroxylated form. In addition to the qualitative analysis of the XRD results, the amorphous content in each sample was estimated through the DOC method combined with the single peak method. Fig. 2 presents the amorphous content depending on the milling time of K, the nine formulations of milling time-rotation speed, and MK. The series with the same rotation speeds follow an exponential increase with rotation time (with very good R^2). Significant growth of the amorphous phase at a constant time with different rotation speeds was also detected. The maximum amorphous content was obtained after grinding at 350 rpm and 120 min (K350–120), around 94 wt%. Raw K already contained an amorphous fraction of approximately 17 wt%. Accordingly, the difference between K and the activated samples is remarkable. The less intensive mechanical treatment (K250–30) presented an increase of more than 30 wt% compared to K, with an amorphous content of almost 50 wt%. With increasing time, the gap of amorphous content between the samples with the same milling time diminished, as almost all
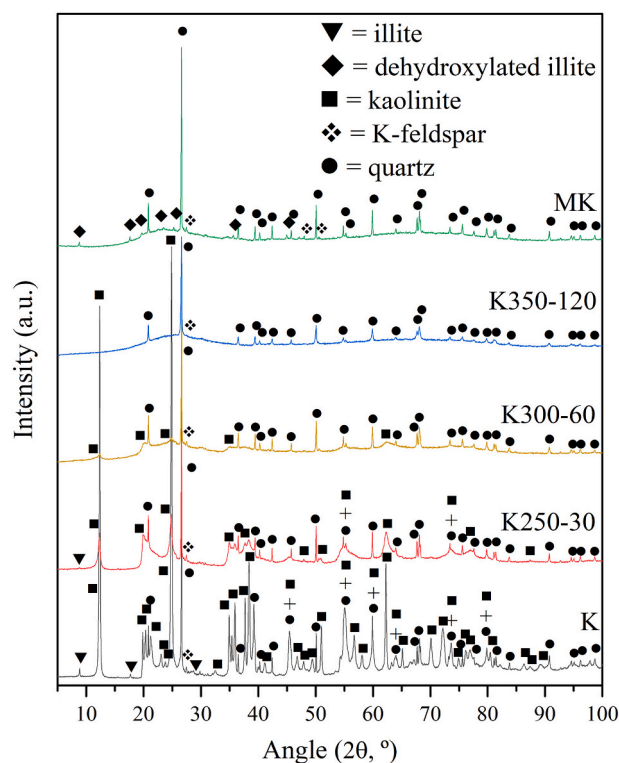

Fig. 1. X-ray powder diffractograms of K, K250–30, K300–60, K350–120, and MK.
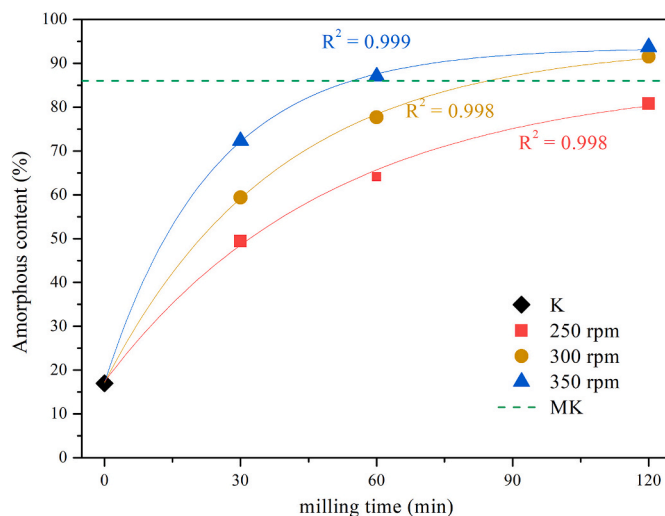

Fig. 2. Amorphous content estimation of the mechanically activated samples, K, and MK.

kaolinite was converted to amorphous phase with higher time and rotation speed. The same trend is observed with the samples with the same rotation speed and different grinding times. The amorphous content of MK was around 86 wt% (dashed line). As aforementioned, the crystalline phases of quartz and K-feldspar remained unaffected with TA, while the dehydroxylated phase of illite is crystalline, meaning that only kaolinite was amorphized. Therefore, the higher amorphous content detected in the MA samples with very aggressive grinding than in MK (92 wt% in K300–120, 87 wt% in K350–60 and 94 wt% in K350–120) was mainly due to the amorphization of illite and some K-feldspar and quartz, aside from kaolinite. Between the samples K350–60, K300–120 and K350–120, there was a slight increase of

amorphous phase that should be due to an increase of K-feldspar's amorphization together with the beginning of quartz's amorphization through particle size reduction (Wan et al., 2020).

Fig. 3a shows the difference between representative MA samples (K250–30 and K350–120), K, and MK in the Al surroundings evaluated with ^{27}Al MAS NMR. K spectrum revealed that almost all Al in the structure was in octahedral positions, 6-coordinated Al (Al^{VI}), with a very intense peak at around 5 ppm. The small peak around 20 ppm could be due to poorly-ordered kaolinite (Izadifar et al., 2020). The peak at 60 ppm is usually observed in feldspars, due to Q^4 Al environments, and may be due to K-feldspars, while the peak at 70 ppm is usually detected in illite, assigned to Al substituting Si in the tetrahedral sheet (Mantovani et al., 2009). The contribution of the small content of the amorphous phase could also be assigned to both peaks. With mechanical treatment (K250–30), the intensity of the Al^{VI} resonance notably diminished compared to K, while some Al was changed to 4-coordination (Al^{IV}). However, the main peak is still assigned to octahedral aluminium, meaning that the environment of aluminium was hardly modified although the structure was disordered. The intensity of the peak at ~70 ppm assigned to illite diminished since illite was mostly amorphized. In contrast, with the most intensive MA (K350–120), the amount of Al^{VI} was much lower than in K and K250–30. The kaolinite structure was highly modified, as also seen in XRD, and the aluminium was mostly tetrahedrally and pentahedrally coordinated, being this last the most reactive form of Al (Ruiz-Santaquiteria and Skibsted, 2015). The appearance of Al at lower coordinations (higher chemical shift) observed after MA is due to the release of hydroxyl groups from the structure. The remaining Al^{VI} could be due to new bonds of Al-O-Si, formed due to the substantial modification of the sheet structure caused by the mechanical treatment or new bonds between particles created through cold-welding. It could also be due to some remaining bonded hydroxyls. In contrast, the Al environment in MK was almost fully changed to 5- and 4-coordination due to the complete elimination of OH groups and the transition from kaolinite to metakaolinite. After dehydroxylation, there is a recombination of the Si and Al from the kaolinite sheets into amorphous SiO$_2$ and Al$_2$O$_3$ (Ptáček et al., 2010). Therefore, unlike with MA, most Al is not bonded to Si through oxygens. Compared to MK, the amount of Al^{VI} in K350–120 was still high. Therefore, the reactivity of MK was expected to be higher than K350–120 and K250–30.

The ^{29}Si spectra of the same samples are shown in Fig. 3b. The spectrum of K presented a very intense signal at around −91.5 ppm, which is consistent with other authors in the bibliography (Massiot et al., 1995; Mantovani et al., 2009; Khabbouchi et al., 2018). This peak is characteristic of layered silicates; a Q^3 environment with the Si atom

coordinated via oxygens with three other Si atoms from other tetrahedra on the same sheet (Si—3Si), and no aluminium in the tetrahedral layer, Q^3(0Al) (Liu et al., 2001; Khabbouchi et al., 2018; Li et al., 2019). The small peak at around −107 ppm was assigned to Q^4 of quartz (Gobindlal et al., 2021). In K250–30, the same kaolinite peak was still observed. However, it is broadened and less intense, and therefore the environment of Si would be slightly affected by MA (Derouiche and Baklouti, 2021). This broadening was due to a partial disordering of the tetrahedral sheet of kaolinite. Since the variation was slight, probably the Q^3 structure was maintained but distorted, maintaining the layered structure. However, in K350–120, the sharp signal at −91.5 ppm was not detected, denoting that the kaolinite layered structure was completely modified. The sharp band was transformed into a broad band centred at −97 ppm. The increase of the width of this band indicates the presence of amorphous phase (He et al., 2003). This new broad band was probably formed due to the contribution of pseudo Q^3 coordination and Q^4 environments of the amorphous phase (Ouyang et al., 2016; Li et al., 2019). In this new band, there is probably a contribution of a Q^4 environment of a Si atom with an environment of 3 Si and 1 Al atoms (Si—3Si,1Al) (Lambert et al., 1989). This assignation is consistent with the explanation that new Si-O-Al bonds could be formed in K350–120. The transition of this band in MK, found at lower values (centred at −105 ppm), means that the Q^3 structure is almost residual, and all the Si is in Q^4 coordination. In contrast with K350–120, the Q^4 contribution of MK is characteristic of Si linked to 4 Si via oxygens in silica polymorphs (Si—4Si); therefore, the contribution of Al in ^{29}Si MAS NMRMK is virtually residual (Lambert et al., 1989; Rocha and Klinowski, 1990). This fact supports the consideration that SiO$_2$ and Al$_2$O$_3$ are not linked in metakaolin (Ptáček et al., 2014). As mentioned above, this could be an important difference between TA and MA, since the bonding of Al and Si could be a drawback of MA samples, causing lower reactivity of mechanically activated kaolin than metakaolin.

The main band of the FTIR spectra (1300–850 cm^{-1}) corresponding to Si—O and Al-OH regions was deconvoluted to investigate the significant modification in kaolin spectrum through grinding and elucidate the process of phase transition from kaolinite to amorphous and more reactive phase through MA and TA. Since there is no bibliography on the subject, the bands were found with the help of the second derivative function of the software and previous knowledge. The assignations were performed based on the knowledge of the samples from the previous analysis and on the wavenumber where the bands were obtained. Through XRD, kaolinite, quartz, K-feldspar and illite were detected, and the vibrations of their characteristic bonds should be detected in the IR spectra. The characteristic vibrations of kaolinite in K were detected at 1114 cm^{-1}, 1031 cm^{-1}, 1008 cm^{-1}, 938 cm^{-1} and 914 cm^{-1}, assigned
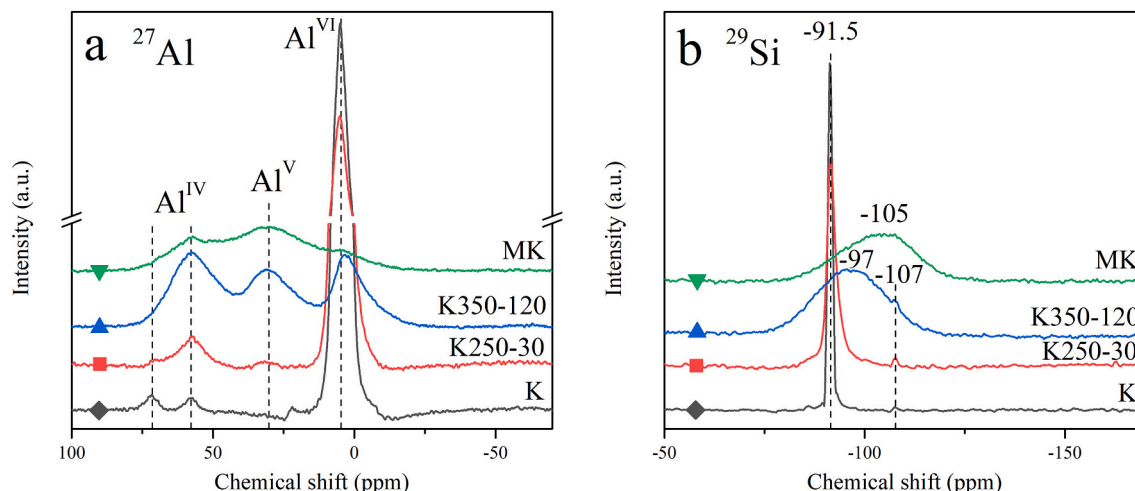

Fig. 3. MAS NMR spectra of (a) ^{27}Al and (b) ^{29}Si for K, K250–30, K350–120, and MK.

to the apical vibrations of apical Si—O bonds, in-plane Si-O-Si stretching vibrations, Si-O-Al vibrations, inner surface hydroxyl groups Al-O-H vibrations and inner O—H vibrations in Al-O-H, respectively (Hoch and Bandara, 2005; Horváth et al., 2010; Li et al., 2019). Si-O-Si bond vibration of quartz is usually detected around 1080 cm^{-1} while here it was detected through deconvolution at around 1076 cm^{-1} (Müller et al., 2014). K-feldspar could not be detected since their main bands at 1090 cm^{-1}, 1050 cm^{-1} and 1010 cm^{-1} corresponding to Si—O (the first band) and Si-O-Al (the following two) were overlapped with some kaolinite and quartz bands, which were much more intense due to their major contribution to the material's composition (Theodosoglou et al., 2017). The same phenomenon was observed with illite. Its characteristic bands detected at 1027 cm^{-1} and 935 cm^{-1} are assigned to Si—O and Al-OH overlapped with kaolinite bands (Jiang et al., 2008). Bands at 1098 cm^{-1}, 1047 cm^{-1} and 997 cm^{-1} were not assigned to crystalline phases and therefore were attributed to poorly ordered kaolinite and amorphous phase, which were the remaining phases in the material. There was probably some contribution to this bands of K-feldspar, quartz and illite as well. Since the contribution of aluminium, with Si-O-Al bonds, is usually detected at lower wavenumbers than Si—O and Si-O-Si, the bands at 1098 cm^{-1} and 1047 cm^{-1} were assigned to non-ordered Si-O-Si and Si—O bonds, while 997 cm^{-1} band was probably caused by Si-O-Al bonds. In Fig. 4b, K250–30, the bands of Si—O bonds in kaolinite were slightly shifted to higher wavenumbers, probably due to modifications in the structure. The intensity of the bands at 1120 cm^{-1}, 1033 cm^{-1} and 1011 cm^{-1} was reduced, but their contribution to the spectra was still relevant, suggesting that kaolinite was still the main phase although a significant part was poorly ordered, which was consistent with the XRD results studied in Fig. 1. Meanwhile, the illite and kaolinite amorphization caused the increase of the intensities and width of 1098 cm^{-1} and 1052 cm^{-1} bands assigned to amorphous material. The Al-OH bonding was also affected; the reduction of 936 cm^{-1} and 914 cm^{-1} bands should be directly related to the separation of hydroxyls from the structure. The spectrum of the K300–60 sample (Fig. 4c) was mainly an overlap of all the bands. Despite some amount of kaolinite or poorly ordered kaolinite could still be detected, most of the material was amorphous. A substantial growth of the bands at 1099 cm^{-1}, 1047 cm^{-1}, and 997 cm^{-1} was detected. Moreover, the amorphous phase was the majority, which agreed with the XRD results. The remaining Si-O-Si and Si—O kaolinite bands at 1120 cm^{-1} and 1011 cm^{-1} were added with the help of the second derivative method of the software since these bands were entirely enclosed within the amorphous bands. For this reason, the band at 1033 cm^{-1} could not be added to the deconvolution. Quartz Si-O-Si at 1080 cm^{-1} was also overlapped with the band assigned to amorphous Si-O-Si at 1099 cm^{-1}. At the Al-OH region, there was still a small contribution of 936 cm^{-1} and 914 cm^{-1} bands from remaining bonded hydroxyls in kaolinite, but with the first band entirely enclosed in the Si-O-Al amorphous band at 997 cm^{-1}. A new band at 1162 cm^{-1} raised, assigned to amorphous Si-O-Si. This new band was probably caused because the Si tetrahedral sheet was highly modified and amorphized with energetic MA. In the K350–120 spectrum (Fig. 4d), the bands corresponding to crystalline phases were fully substituted by the amorphous phases also detected in the previous samples, with a small band at 1093 cm^{-1} that could be due to quartz Si-O-Si bonds, despite being displaced to higher wavenumber. This displacement could be due to the modification of quartz structure after intensive mechanical treatments, also observed through XRD (Fig. 1). This band assigned to quartz maintained approximately the same relative width and intensity through all the mechanical treatments except after 350 rpm for 120 min of MA, K350–120 (Fig. 4d). This fact could be either due to a complete overlap of the bands that masks the quartz band even with the help of the second derivative or to a quartz content reduction as suggested by the XRD results. The bands corresponding to Al-OH bonds were no longer detected, meaning that all the hydroxyls were probably not bonded to the new amorphous structure. For MK (Fig. 4e), the spectrum maximum was centred at higher wavenumbers since there is a
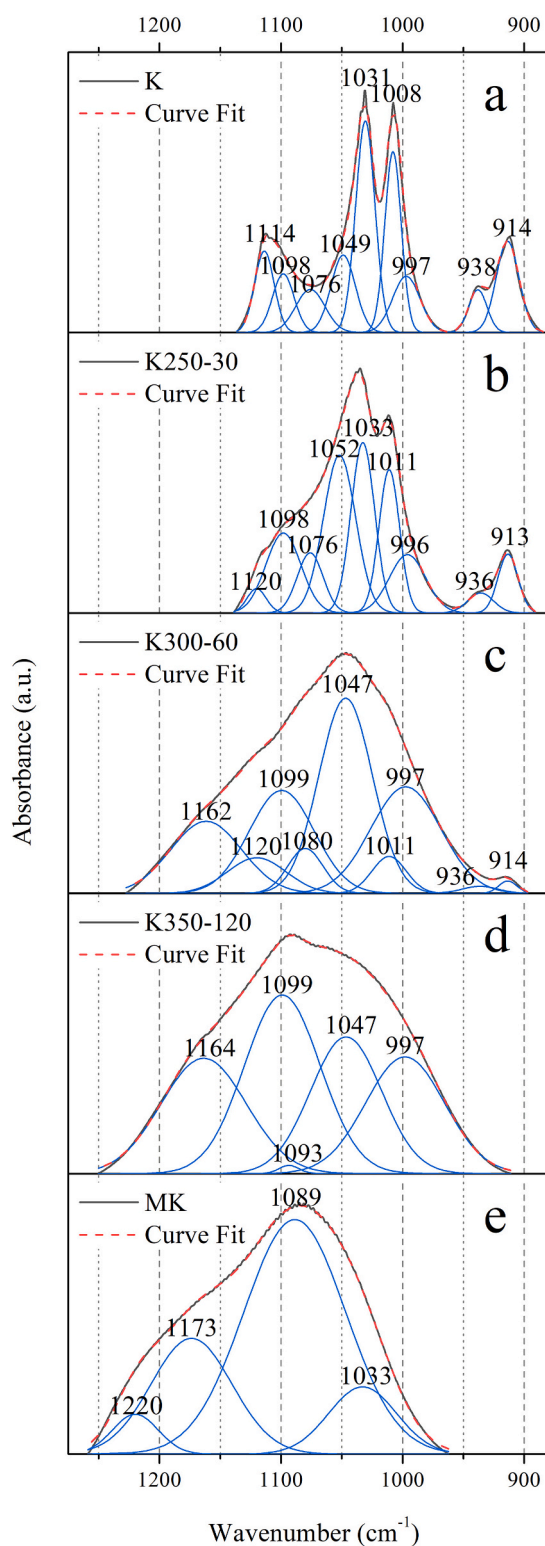

Fig. 4. FTIR deconvolution of (a) K, (b) K250–30, (c) K300–60, (d) K350–120, (e) MK in the 1300–850 cm^{-1} range.

significant contribution of Si-O-Si bonds. As explained before, the metakaolin is formed through recombination of Si and Al environments to form Al$_2$O$_3$ and SiO$_2$ that are not strongly bonded between them, explaining that there is probably almost no contribution of Si-O-Al bonds. The deconvolution band centred at 1033 cm^{-1} could comprehend the contribution of some Si-O-Al bonds from K-feldspar and dehydroxylated illite. All the other bands were assigned to Si—O and Si-

O-Si bonds from metakaolin. The bands at 1173 cm^{-1} and 1220 cm^{-1} were assigned to the shoulders of the main Si-O-Si asymmetric stretching band at 1089 cm^{-1} (Lee and Van Deventer, 2003; Zhang et al., 2012; El-Naggar and El-Dessouky, 2017). The Si-O-Si of quartz was not likely detected due to the overlapping bands with much more intensity.

The potential reactivity of the samples was quantified through chemical extractions with NaOH 8 M. This test is mostly used to evaluate the potentially reactive precursors for geopolymers and alkali-activated materials but could also be suitable for other cement types. The potentially reactive SiO_2 and Al_2O_3 was studied since these oxides are essential during the gelation process and formation of cementitious phases. The results obtained are not the total amount of oxides that would react in cement, but the potentially reactive oxides, since the amount of alkali used in the test is substantially higher than in a cement curing process, making the environment much more aggressive. Depending on the formulation of the cement, a larger or smaller part of the results exposed herein will react. Fig. 5 presents the results of potentially reactive SiO_2 (dark grey) and Al_2O_3 (light grey) expressed in wt% of the total SiO_2 and Al_2O_3 extracted from XRF results of the raw kaolin. For MK, the results were compared to the percentages of oxides in calcined kaolin. In K, around 40 wt% of the total SiO_2 and 50 wt% of the total Al_2O_3 was potentially reactive. The dissolved SiO_2 and Al_2O_3 in K should be the amorphous and disordered kaolinite. Probably part of kaolinite was also solubilized in this very aggressive NaOH medium. However, this amount would be significantly lower in a geopolymer or a conventional cement formulation since the liquid-to-solid ratio is much lower. With the less energetic MA (K250–30), the amount of solubilized oxides notably increased, increases of 44 wt% for SiO_2 and 40 wt% for Al_2O_3. Intensifying the MA, the dissolved amount of SiO_2 increased even more, from 86 wt% in K250–30 to 96 wt% in K350–120. The Al_2O_3 increase was lower but remarkable, 88 wt% to 94 wt%. The results indicate that almost all the SiO_2 and Al_2O_3 from raw kaolin was dissolved and potentially reactive in a strongly alkaline solution. The total amount of SiO_2 and Al_2O_3 dissolved in MK was also remarkable, 92 and 93 wt%, respectively. It is noteworthy that the amount of dissolved SiO_2 and Al_2O_3 in MK was slightly lower than in K350–120, around 4 wt% and 1 wt%, respectively. This result implies that through MA, illite and some K-feldspars and quartz were activated, as previously suggested, and therefore reactive in a strongly aggressive alkaline environment. The results also agreed with the amorphous content estimation in Fig. 2, meaning that, as expected, p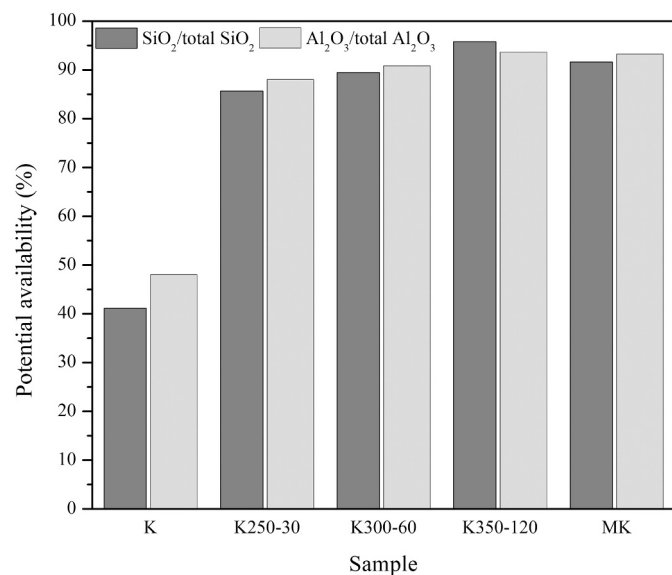robably almost all the amorphous phase is potentially reactive. In this sense, the insoluble residue was also evaluated to identify the remaining crystalline phases after the chemical attacks.

The XRD diffractograms of the insoluble residue were studied to elucidate the potentially reactive and non-reactive phases (Fig. 6). The unreacted residue was referred to the sample name, hyphen NaOH (e.g. K insoluble residue would be K-NaOH). For K, the dissolved oxides detected through ICP-OES (Fig. 5) were possibly due mainly to some partially disordered kaolinite and weak parts of its structure, aside from the small amorphous phase detected in Fig. 2. Despite some SiO_2 and Al_2O_3 being dissolved, kaolinite was still the main crystalline phase of K-NaOH. Quartz, K-feldspar and illite were detected as well and remained unaffected. The most remarkable difference compared to XRD results of the MA and TA samples before the chemical attack (Fig. 1), is that the amorphous content in the residue of all the samples after the chemical attack was drastically reduced, as the halo was reduced to a nearly flat line. K250–30-NaOH also presented some kaolinite content in the unreacted solid, but it is a minority. Compared to K250–30 (sample before the alkaline attack), the kaolinite content appears to be much lower. This fact means that with this MA, the kaolinite was not fully transformed to amorphous phase, but its structure was weakened enough to be dissolved in the NaOH 8 M solution since most of the remaining kaolinite was solubilized. The reduction of particle size through grinding could make kaolinite more reactive. The small kaolinite content detected in K300–60 before the chemical attack was nearly totally dissolved since kaolinite was practically not discernible in the diffractogram of K300–60-NaOH. K350–120-NaOH did not present kaolinite, and K-feldspar reflections were significantly lower than in the residues of the other samples, meaning that probably was partially solubilized. Quartz reflections were also lower in intensity, most likely implying that some quartz was dissolved (in agreement with the high amount of dissolved SiO_2 detected through ICP-OES). MK-NaOH presented unaltered quartz, K-feldspar and dehydroxylated illite as in MK, indicating that the only dissolved phase was metakaolinite. The presence of dehydroxylated illite in the insoluble residue confirms that it is not a potentially reactive phase, while with MA, illite was amorphized and dissolved. All the samples also presented a new crystalline phase assigned to Na_2CO_3, which was generated due to NaOH surplus and atmospheric CO_2 reaction.

Fig. 7 compares the FTIR spectra of the insoluble residues and the samples before the chemical attack in the 1500–700 cm^{-1} range. Similarly to XRD results, the FTIR spectrum of K-NaOH (Fig. 7a) was the same as K with some variations in bands' intensity. The assignation of the bands was previously discussed in Fig. 4. Two additional bands were detected at all the insoluble residues of the chemical attacks except K-NaOH. A broad and intense band around 1454 cm^{-1} and a sharp and less intense band at ~880 cm^{-1}, assigned to the asymmetric stretching and bending of carbonates O-C-O vibrations from Na_2CO_3, respectively (Li et al., 2017; Shi et al., 2018). In K250–30-NaOH (Fig. 7b), the amount of kaolinite remaining after the chemical attack was smaller, meaning that the kaolinite solubilized was probably partially disordered. This caused a change in the spectrum compared to K250–30. The band assigned to quartz at around 1080 cm^{-1} was more intense since its weight percentage was higher after dissolving the potentially reactive phases. However, the main bands of kaolinite were still detected since the residue presented unreacted kaolinite, which was also detected through XRD. K300–60-NaOH (Fig. 7c) did not present the bands of kaolinite. The spectrum presented a wide band with a maximum at ~1088 cm^{-1} corresponding to Si-O-Si of quartz and a broad shoulder at ~1020 cm^{-1} probably corresponding to an overlap of K-feldspar and some remaining kaolinite Si—O bonds, which were also the remaining crystalline phases detected through XRD. However, in K300–60-NaOH, the maximum was found at the wavenumber of quartz Si-O-Si vibrations since kaolinite content was almost irrelevant compared to K300–60. In K350–120-NaOH (Fig. 7d), the band corresponding to Si-O-Si of quartz at 1095 cm^{-1} presented higher intensity since K-feldspar was partially dissolved
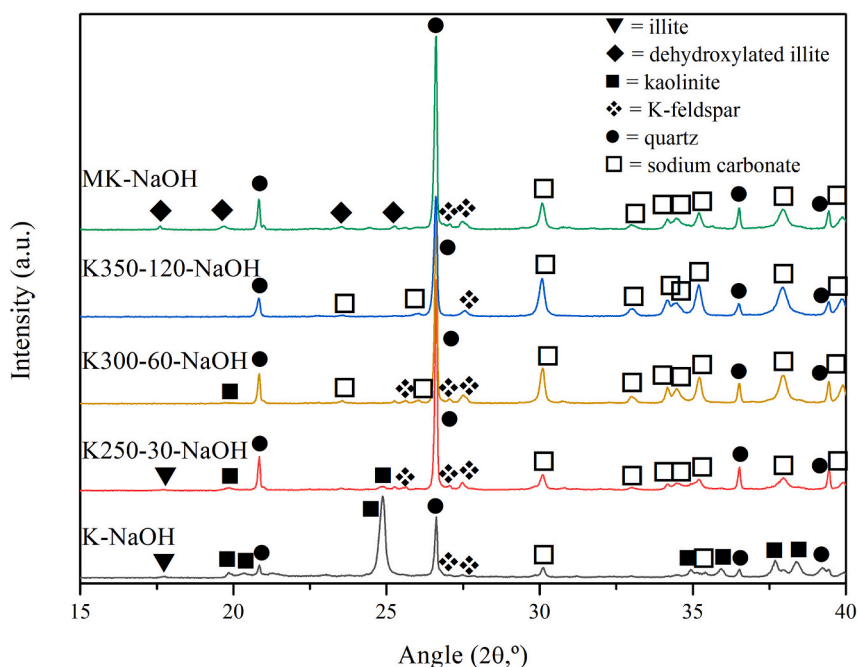

Fig. 5. Potential availability of SiO_2 and Al_2O_3 expressed in percentage from the total SiO_2 and Al_2O_3 of the sample determined through XRF.

Fig. 6. X-ray powder diffractograms of the insoluble residues of the NaOH 8 M chemical attacks.

in the solution. Therefore, quartz was the main phase of the material, together with Na_2CO_3. The small contribution of the K-feldspar was probably masked due to overlapping. The band of MK-NaOH (Fig. 7e) was remarkably shifted to lower wavenumbers compared to MK. This was because the spectrum presented a wide band formed by overlapping dehydroxylated illite Si—O at ~1026 cm^{-1}, detected in illite samples (Yang et al., 2005; Jiang et al., 2008), and quartz and illite Si-O-Si at ~1089 cm^{-1}. Furthermore, K-feldspar Si—O and Si-O-Al vibrations were also probably overlapped in the wide band. The broad band detected at around 800 cm^{-1} in MK, assigned to metakaolinite Al^{IV}-O bonds, was not detected in MK-NaOH, meaning that metakaolinite was fully dissolved in the alkaline solution. The band at 1165 cm^{-1} detected in all the insoluble residues was assigned to Si—O stretching vibration of quartz, while the characteristic doublet at 798 and 779 cm^{-1} was due to Si-O-Si inter-tetrahedral bonds (Souri et al., 2015; Udvardi et al., 2017). A displacement to higher wavenumbers was detected in the quartz band at ~1080 cm^{-1} with increasing MA. In MK-NaOH and K250–30-NaOH, the band was detected at 1080–1085 cm^{-1}, while in K300–60-NaOH and K350–120-NaOH, it was detected at 1088 cm^{-1} and 1095 cm^{-1}, respectively. This displacement may likely be due to a variation in the quartz bonds caused by the intensive grinding and particle size reduction (Udvardi et al., 2017).

4. Conclusions

This study evaluated the potential applicability of mechanically activated kaolin as alternative cementitious material (ACM) precursor or supplementary cementitious material (SCM). The structural modifications induced from the mechanical treatments were supervised through different original characterization techniques. Furthermore, the potential reactivity of the activated kaolins was quantified through alkaline chemical attacks. The results were compared to raw kaolin and metakaolin, produced through thermal activation (TA) of the same raw kaolin, as reference materials. The following conclusions were obtained from this work:

- Kaolin undergoes a complete structural transformation derived from mechanical activation (MA). The main phase kaolinite is completely amorphized with intensive mechanical treatments. Compared to MK,

higher amorphous content was reached in some MA samples since the impurities (illite, quartz and K-feldspars) were also amorphized or partially amorphized. Therefore, a more reactive phase could be obtained. The amorphization process can be reasonably well monitored with Fourier-transform infrared spectroscopy (FTIR) through the deconvolution of the Si-O/Al-OH band. The bands assigned to kaolinite were drastically reduced as new bands assigned to amorphous material raised.

- Despite the high amorphous content, some of the aluminium in MA samples remained in octahedral form, which is less reactive than tetrahedral and pentahedral aluminium. This fact could be a drawback in cement formulation since octahedral aluminium may stand unreacted. Moreover, Si-O-Al bonds were probably formed or not removed with MA, which is a remarkable distinction to MK, where Si tetrahedra are in a Q^4 environment surrounded only by Si tetrahedra, and all Al was 4- or 5-coordinated.

- The potential reactivity of MA samples, quantified through alkaline chemical attacks, was comparable to MK and, in the most aggressive mechanical treatment, even higher. This results support that the estimated amorphous content is potentially reactive. The amount of dissolved SiO_2 and Al_2O_3 was slightly higher than in MK due to the amorphization of illite and some K-feldspar and quartz.

- By investigating the insoluble residue of the chemical attacks (not reacting material), the non-reactive phases could be determined. Crystalline quartz and K-feldspar remained unaltered except in the samples with the most energetic MA. Some crystalline kaolinite reacted since the intensity of the reflections in X-ray diffraction (XRD) was lower than before chemical attacks. This phenomenon could be due to a particle size reduction caused by grinding or to partial disorder in kaolinite lattice, which weakens the structure. In MK, the dehydroxylated form of illite did not react since it was observed in the insoluble residue.

The results obtained in this study provide a clear picture of the reactivity of mechanically activated kaolin. The amorphous content increase was validated through XRD, FTIR deconvolution and chemical attacks characterization techniques. The synergistic combination of the chemical attacks and the monitorization through XRD and FTIR deconvolution could become an interesting tool to determine the
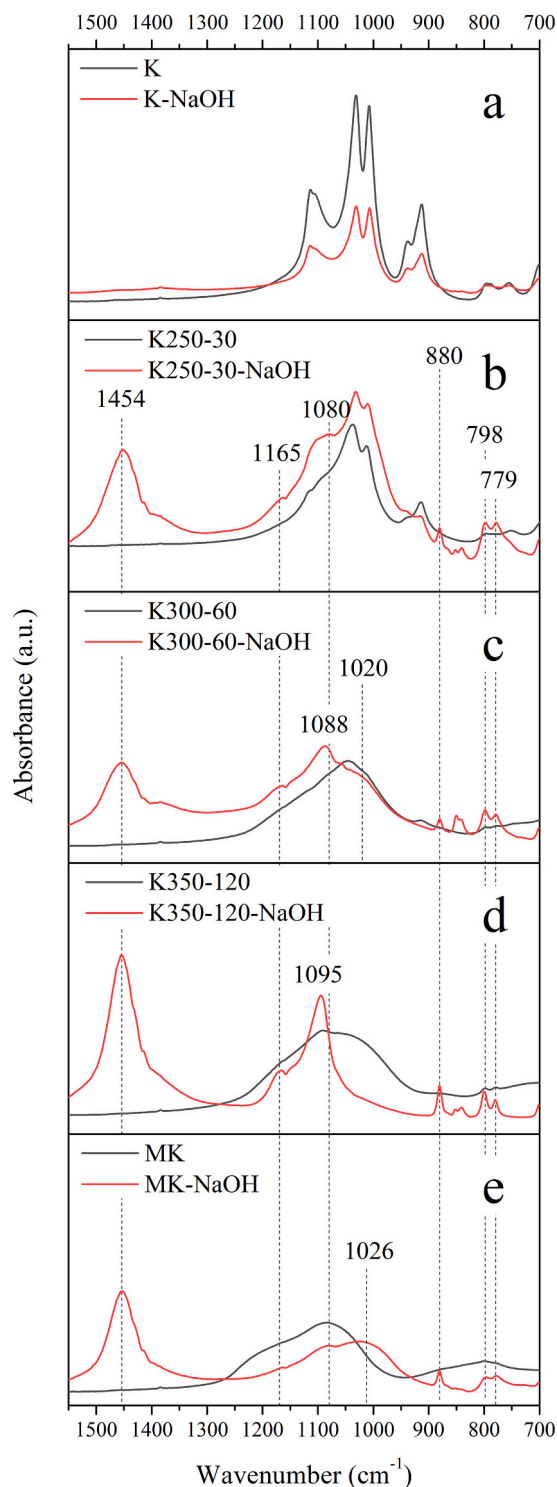
Fig. 7. FTIR spectra of the insoluble residues of the NaOH 8 M chemical attacks (a) K vs K-NaOH, (b) K250–30 vs K250–30-NaOH, (c) K300–60 vs K300–60-NaOH, (d) K350–120 vs K350–120-NaOH, (e) MK vs MK-NaOH in the 1550–700 cm^{-1} range.

reactivity of based-clay materials. The future research on the mechanically activated kaolin's reactivity should be focused on the full transformation of 6-coordinated Al to 4- and 5-coordinated Al to maximize the material's reactivity, and its evaluation as SCM through pozzolanic activity tests.

Declaration of Competing Interest

No.

Data availability

Data will be made available on request.

References

Akhgar, B.N., Pourghahramani, P., 2015. Impact of mechanical activation and mechanochemical activation on natural pyrite dissolution. Hydrometallurgy 153, 83–87. https://doi.org/10.1016/j.hydromet.2015.02.010.

Baláž, P., 2008. Mechanochemistry in Nanoscience and Minerals Engineering. Springer, Berlin. https://doi.org/10.1007/978-3-540-74855-7.

Baláž, P., Achimovicová, M., Baláž, M., Billik, P., Zara, C.Z., Criado, J.M., Delogu, F., Dutková, E., Gaffet, E., Gotor, F.J., Kumar, R., Mitov, I., Rojac, T., Senna, M., Streletskii, A., Krystyna, W.C., 2013. Hallmarks of mechanochemistry: from nanoparticles to technology. Chem. Soc. Rev. 42, 7571–7637. https://doi.org/10.1039/c3cs35468g.

Balczár, I., Korim, T., Kovács, A., Makó, E., 2016. Mechanochemical and thermal activation of kaolin for manufacturing geopolymer mortars – Comparative study. Ceram. Int. 42, 15367–15375. https://doi.org/10.1016/j.ceramint.2016.06.182.

Bergaya, F., Lagaly, G., 2006. General introduction: Clays, clay minerals, and clay science. In: Handbook of Clay Science, pp. 1–18. https://doi.org/10.1016/S1572-4352(05)01001-9.

Cheng, Y., Xing, J., Bu, C., Zhang, J., Piao, G., Huang, Y., Xie, H., Wang, X., 2019. Dehydroxylation and structural distortion of kaolinite as a high-temperature sorbent in the furnace. Minerals 9. https://doi.org/10.3390/min9100587.

Daou, I., Lecomte-Nana, G.L., Tessier-Doyen, N., Peyratout, C., Gonon, M.F., Guinebretiere, R., 2020. Probing the dehydroxylation of kaolinite and halloysite by in situ high temperature x-ray diffraction. Minerals 10. https://doi.org/10.3390/min10050480.

Derouiche, R., Baklouti, S., 2021. Phosphoric acid based geopolymerization: effect of the mechanochemical and the thermal activation of the kaolin. Ceram. Int. 47, 13446–13456. https://doi.org/10.1016/j.ceramint.2021.01.203.

El-Naggar, M.R., El-Dessouky, M.I., 2017. Re-use of waste glass in improving properties of metakaolin-based geopolymers: mechanical and microstructure examinations. Constr. Build. Mater. 132, 543–555. https://doi.org/10.1016/j.conbuildmat.2016.12.023.

Fitos, M., Badogiannis, E.G., Tsivilis, S.G., Perraki, M., 2015. Pozzolanic activity of thermally and mechanically treated kaolins of hydrothermal origin. Appl. Clay Sci. 116–117, 182–192. https://doi.org/10.1016/j.clay.2015.08.028.

Gobindlal, K., Zujovic, Z., Yadav, P., Sperry, J., Weber, C.C., 2021. The mechanism of surface-radical generation and amorphization of crystalline quartz sand upon mechanochemical grinding. J. Phys. Chem. C 125, 20877–20886. https://doi.org/10.1021/acs.jpcc.1c06069.

He, H.P., Guo, J.G., Zhu, J.X., Hu, C., 2003. ^{29}Si and ^{27}Al MAS NMR study of the thermal transformations of kaolinite from North China. Clay Miner. 38, 551–559. https://doi.org/10.1180/0009855033840114.

Hoch, M., Bandara, A., 2005. Determination of the adsorption process of tributyltin (TBT) and monobutyltin (MBT) onto kaolinite surface using Fourier transform infrared (FTIR) spectroscopy. Colloids Surfaces A Physicochem. Eng. Asp. 253, 117–124. https://doi.org/10.1016/j.colsurfa.2004.10.118.

Horváth, E., Kristóf, J., Frost, R.L., 2010. Vibrational spectroscopy of intercalated kaolinites. Part I. Appl. Spectrosc. Rev. 45, 130–147. https://doi.org/10.1080/05704920903435862.

Hounsi, A.D., Lecomte-Nana, G.L., Djétéli, G., Blanchart, P., 2013. Kaolin-based geopolymers: effect of mechanical activation and curing process. Constr. Build. Mater. 42, 105–113. https://doi.org/10.1016/j.conbuildmat.2012.12.069.

Izadifar, M., Thissen, P., Steudel, A., Kleeberg, R., Kaufhold, S., Kaltenbach, J., Schuhmann, R., Dehn, F., Emmerich, K., 2020. Comprehensive examination of dehydroxylation of kaolinite, disordered kaolinite, and dickite: experimental studies and density functional theory. Clay Clay Miner. 68, 319–333. https://doi.org/10.1007/s42860-020-00082-w.

Jiang, T., Li, G., Qiu, G., Fan, X., Huang, Z., 2008. Thermal activation and alkali dissolution of silicon from illite. Appl. Clay Sci. 40, 81–89. https://doi.org/10.1016/j.clay.2007.08.002.

Juenger, M.C.G., Siddique, R., 2015. Recent advances in understanding the role of supplementary cementitious materials in concrete. Cem. Concr. Res. 78, 71–80. https://doi.org/10.1016/j.cemconres.2015.03.018.

Juenger, M.C.G., Winnefeld, F., Provis, J.L., Ideker, J.H., 2011. Advances in alternative cementitious binders. Cem. Concr. Res. 41, 1232–1243. https://doi.org/10.1016/j.cemconres.2010.11.012.

Juenger, M.C.G., Snellings, R., Bernal, S.A., 2019. Supplementary cementitious materials: new sources, characterization, and performance insights. Cem. Concr. Res. 122, 257–273. https://doi.org/10.1016/j.cemconres.2019.05.008.

Khabbouchi, M., Hosni, K., Srasra, E., 2018. Physico-chemical characterization of modified tunisian kaolin by phosphoric acid. Surf. Eng. Appl. Electrochem. 54, 219–226. https://doi.org/10.3103/S1068375518020072.

Khalifa, A.Z., Cizer, Ö., Pontikes, Y., Heath, A., Patureau, P., Bernal, S.A., Marsh, A.T.M., 2020. Advances in alkali-activation of clay minerals. Cem. Concr. Res. 132, 106050 https://doi.org/10.1016/j.cemconres.2020.106050.

Kuenzel, C., Ranjbar, N., 2019. Dissolution mechanism of fly ash to quantify the reactive aluminosilicates in geopolymerisation. Resour. Conserv. Recycl. 150, 104421 https://doi.org/10.1016/j.resconrec.2019.104421.

Lambert, J.F., Millman, W.S., Fripiat, J.J., 1989. Revisiting kaolinite dehydroxylation: a ^{29}Si and ^{27}Al mas NMR study. J. Am. Chem. Soc. 111, 3517–3522. https://doi.org/10.1021/ja00192a005.

Lee, W.K.W., Van Deventer, J.S.J., 2003. Use of infrared spectroscopy to study geopolymerization of heterogeneous amorphous aluminosilicates. Langmuir 19, 8726–8734. https://doi.org/10.1021/la026127e.

Li, J., Zuo, X., Zhao, X., Ouyang, J., Yang, H., 2019. Insight into the effect of crystallographic structure on thermal conductivity of kaolinite nanoclay. Appl. Clay Sci. 173, 12–18. https://doi.org/10.1016/j.clay.2019.03.011.

Li, N., Farzadnia, N., Shi, C., 2017. Microstructural changes in alkali-activated slag mortars induced by accelerated carbonation. Cem. Concr. Res. 100, 214–226. https://doi.org/10.1016/j.cemconres.2017.07.008.

Liew, Y.-M., Heah, C.-Y., Mohd Mustafa, A.B., Kamarudin, H., 2016. Structure and properties of clay-based geopolymer cements: a review. Prog. Mater. Sci. 83, 595–629. https://doi.org/10.1016/j.pmatsci.2016.08.002.

Liu, Qinfu, Spears, D.A., Liu, Qinpu, 2001. MAS NMR study of surface-modified calcined kaolin. Appl. Clay Sci. 19, 89–94. https://doi.org/10.1016/S0169-1317(01)00057-6.

Lothenbach, B., Scrivener, K., Hooton, R.D., 2011. Supplementary cementitious materials. Cem. Concr. Res. 41, 1244–1256. https://doi.org/10.1016/j.cemconres.2010.12.001.

Madsen, I.C., Scarlett, N.V.Y., Kern, A., 2011. Description and survey of methodologies for the determination of amorphous content via X-ray powder diffraction. Z. Krist. 226, 944–955. https://doi.org/10.1524/zkri.2011.1437.

Mañosa, J., Cerezo-Piñas, M., Maldonado-Alameda, A., Formosa, J., Giro-Paloma, J., Rosell, J.R., Chimenos, J.M., 2021. Water treatment sludge as precursor in non-dehydroxylated kaolin-based alkali-activated cements. Appl. Clay Sci. 204 https://doi.org/10.1016/j.clay.2021.106032.

Mantovani, M., Escudero, A., Becerro, A.I., 2009. Application of ^{29}Si and ^{27}Al MAS NMR spectroscopy to the study of the reaction mechanism of kaolinite to illite/muscovite. Clay Clay Miner. 57, 302–310. https://doi.org/10.1346/CCMN.2009.0570303.

Massiot, D., Dion, P., Alcober, J.F., Bergaya, F., 1995. ^{27}Al and ^{29}Si NMR study of kaolinite thermal decomposition by controlled rate thermal analysis. J. Am. Ceram. Soc. 78, 2940–2944. https://doi.org/10.1111/j.1151-2916.1995.tb09067.x.

Mitrović, A., Zdujić, M., 2014. Preparation of pozzolanic addition by mechanical treatment of kaolin clay. Int. J. Miner. Process. 132, 59–66. https://doi.org/10.1016/j.minpro.2014.09.004.

Müller, C.M., Pejcic, B., Esteban, L., Piane, C.D., Raven, M., Mizaikoff, B., 2014. Infrared attenuated total reflectance spectroscopy: an innovative strategy for analyzing mineral components in energy relevant systems. Sci. Rep. 4, 1–11. https://doi.org/10.1038/srep06764.

Ondruška, J., Csáki, Š., Trnovcová, V., Štubňa, I., Lukáč, F., Pokorný, J., Vozár, L., Dobroň, P., 2018. Influence of mechanical activation on DC conductivity of kaolin. Appl. Clay Sci. 154, 36–42. https://doi.org/10.1016/j.clay.2017.12.038.

Ouyang, J., Guo, B., Fu, L., Yang, H., Hu, Y., Tang, A., Long, H., Jin, Y., Chen, J., Jiang, J., 2016. Radical guided selective loading of silver nanoparticles at interior lumen and out surface of halloysite nanotubes. Mater. Des. 110, 169–178. https://doi.org/10.1016/j.matdes.2016.07.127.

Provis, J.L., 2018. Alkali-activated materials. Cem. Concr. Res. 114, 40–48. https://doi.org/10.1016/j.cemconres.2017.02.009.

Ptáček, P., Kubátová, D., Havlica, J., Brandštetr, J., Šoukal, F., Opravil, T., 2010. The non-isothermal kinetic analysis of the thermal decomposition of kaolinite by thermogravimetric analysis. Powder Technol. 204, 222–227. https://doi.org/10.1016/j.powtec.2010.08.004.

Ptáček, P., Frajkorová, F., Šoukal, F., Opravil, T., 2014. Kinetics and mechanism of three stages of thermal transformation of kaolinite to metakaolinite. Powder Technol. 264, 439–445. https://doi.org/10.1016/j.powtec.2014.05.047.

Rashad, A.M., 2013. Metakaolin as cementitious material: history, scours, production and composition-a comprehensive overview. Constr. Build. Mater. 41, 303–318. https://doi.org/10.1016/j.conbuildmat.2012.12.001.

Rocha, J., Klinowski, J., 1990. ^{29}Si and ^{27}Al magic-angle-spinning NMR studies of the thermal transformation of kaolinite. Phys. Chem. Miner. 17, 179–186. https://doi.org/10.1007/BF00199671.

Ruiz-Santaquiteria, C., Skibsted, J., Scrivener, K., 2015. Identification of reactive sites in calcined kaolinite and montmorillonite from a combination of chemical methods and solid-state NMR spectroscopy. In: Favier, A. (Ed.), Calcined Clays for Sustainable Concrete. RILEM, pp. 125–132. https://doi.org/10.1007/978-94-024-1207-9_65.

Ruiz-Santaquiteria, C., Fernández-Jiménez, A., Palomo, A., 2011. Quantitative determination of reactive SiO_2 and Al_2O_3 in aluminosilicate materials. 13th Int. Congr. Chem. Cem. 1–7.

San Cristóbal, A.G., Castelló, R., Martín Luengo, M.A., Vizcayno, C., 2010. Zeolites prepared from calcined and mechanically modified kaolins. A comparative study. Appl. Clay Sci. 49, 239–246. https://doi.org/10.1016/j.clay.2010.05.012.

Scrivener, K., Martirena, F., Bishnoi, S., Maity, S., 2018. Calcined clay limestone cements (LC3). Cem. Concr. Res. 114, 49–56. https://doi.org/10.1016/j.cemconres.2017.08.017.

Scrivener, K.L., Kirkpatrick, R.J., 2008. Innovation in use and research on cementitious material. Cem. Concr. Res. 38, 128–136. https://doi.org/10.1016/j.cemconres.2007.09.025.

Sharma, M., Bishnoi, S., Martirena, F., Scrivener, K., 2021. Limestone calcined clay cement and concrete: a state-of-the-art review. Cem. Concr. Res. 149, 106564 https://doi.org/10.1016/j.cemconres.2021.106564.

Shi, C., Qu, B., Provis, J.L., 2019. Recent progress in low-carbon binders. Cem. Concr. Res. 122, 227–250. https://doi.org/10.1016/j.cemconres.2019.05.009.

Shi, Z., Shi, C., Wan, S., Li, N., Zhang, Z., 2018. Effect of alkali dosage and silicate modulus on carbonation of alkali-activated slag mortars. Cem. Concr. Res. 113, 55–64. https://doi.org/10.1016/j.cemconres.2018.07.005.

Souri, A., Kazemi-Kamyab, H., Snellings, R., Naghizadeh, R., Golestani-Fard, F., Scrivener, K., 2015. Pozzolanic activity of mechanochemically and thermally activated kaolins in cement. Cem. Concr. Res. 77, 47–59. https://doi.org/10.1016/j.cemconres.2015.04.017.

Theodosoglou, E., Koroneos, A., Soldatos, T., Zorba, T., Paraskevopoulos, K.M., 2017. Comparative fourier transform infrared and X-Ray powder diffraction analysis of naturally occurred K-Feldspars. Bull. Geol. Soc. Greece 43, 2752. https://doi.org/10.12681/bgsg.11681.

Tole, I., Habermehl-Cwirzen, K., Cwirzen, A., 2019. Mechanochemical activation of natural clay minerals: an alternative to produce sustainable cementitious binders – review. Mineral. Petrol. 113, 449–462. https://doi.org/10.1007/s00710-019-00666-y.

Udvardi, B., Kovács, I.J., Fancsik, T., Kónya, P., Bátori, M., Stercel, F., Falus, G., Szalai, Z., 2017. Effects of particle size on the attenuated total reflection spectrum of minerals. Appl. Spectrosc. 71, 1157–1168. https://doi.org/10.1177/0003702816670914.

Wan, Q., Zhang, Y., Zhang, R., 2020. Using mechanical activation of quartz to enhance the compressive strength of metakaolin based geopolymers. Cem. Concr. Compos. 111, 103635 https://doi.org/10.1016/j.cemconcomp.2020.103635.

Whitfield, P.S., Mitchell, L.D., 2003. Quantitative rietveld analysis of the amorphous content in cements and clinkers. J. Mater. Sci. 38, 4415–4421. https://doi.org/10.1023/A:1026363906432.

Wu, F., Li, H., Yang, K., 2021. Effects of mechanical activation on physical and chemical characteristics of coal-gasification slag. Coatings 11. https://doi.org/10.3390/coatings11080902.

Yang, H., Yang, W., Hu, Y., Du, C., Tang, A., 2005. Effect of mechanochemical processing on illite particles. Part. Part. Syst. Charact. 22, 207–211. https://doi.org/10.1002/ppsc.200500953.

Yanguatin, H., Tobón, J., Ramírez, J., 2017. Pozzolanic reactivity of kaolin clays, a review | Reactividad puzolánica de arcillas caoliníticas, una revisión. Rev. Ing. Constr. 32, 13–24. https://doi.org/10.4067/s0718-50732017000200002.

Zhang, Z., Wang, H., Provis, J.L., Bullen, F., Reid, A., Zhu, Y., 2012. Quantitative kinetic and structural analysis of geopolymers. Part 1. The activation of metakaolin with sodium hydroxide. Thermochim. Acta 539, 23–33. https://doi.org/10.1016/j.tca.2012.03.021.